JASA ARTICLE

Measurements of open-water arctic ocean noise directionality and transport velocity[a)]

Aaron M. Thode,[1,b)] Robert G. Norman,[2] Alexander S. Conrad,[2] Ludovic Tenorio-Hallé,[1] Susanna B. Blackwell,[2,c)] and Katherine H. Kim[2]

[1]*Marine Physical Laboratory, Scripps Institution of Oceanography, University of California San Diego, La Jolla, California 92093-0238, USA*

[2]*Greeneridge Sciences, Inc., 5266 Hollister Ave, Suite 107, Santa Barbara, California 93111, USA*

ABSTRACT:

Measurements from bottom-mounted acoustic vector sensors, deployed seasonally between 2008 and 2014 on the shallow Beaufort Sea shelf along the Alaskan North Slope, are used to estimate the ambient sound pressure power spectral density, acoustic transport velocity of energy, and dominant azimuth between 25 and 450 Hz. Even during ice-free conditions, this region has unusual acoustic features when compared against other U.S. coastal regions. Two distinct regimes exist in the diffuse ambient noise environment: one with high pressure spectral density levels but low directionality, and another with lower spectral density levels but high directionality. The transition between the two states, which is invisible in traditional spectrograms, occurs between 73 and 79 dB re 1 μPa^2/Hz at 100 Hz, with the transition region occurring at lower spectral levels at higher frequencies. Across a wide bandwidth, the high-directionality ambient noise consistently arrives from geographical azimuths between 0° and 30° from true north over multiple years and locations, with a seasonal interquartile range of 40° at low frequencies and high transport velocities. The long-term stability of this directional regime, which is believed to arise from the dominance of wind-driven sources along an east–west coastline, makes it an important feature of arctic ambient sound.

 https://doi.org/10.1121/10.0006206

(Received 17 March 2021; revised 10 August 2021; accepted 19 August 2021; published online 16 September 2021)

[Editor: Hanne Sagen] Pages: 1954–1966

I. INTRODUCTION

Passive underwater acoustic vector sensors have the ability to estimate both acoustic pressure and vector particle velocity from a single point (D'Spain *et al.*, 1991; Nehorai and Paldi, 1994; Deal, 2018). Two-dimensional particle velocity sensors have been incorporated inside Directional Frequency and Recording (DIFAR) sonobuoys for decades (Holler, 2014), as well as commercial autonomous recording packages, such as the Directional Autonomous Seafloor Acoustic Recorder (DASAR), which is built by Greeneridge Sciences Inc. (Goleta, CA) (Greene *et al.*, 2004; Raghukumar *et al.*, 2020). More recent versions of these sensors have been designed with increased monitoring bandwidth (Shipps and Deng, 2003) and sensitivity along three dimensions. Vector sensors have advantages over conventional hydrophones in terms of array gain (Cray and Nuttall, 2001; D'Spain *et al.*, 2006), directional noise suppression (Thode *et al.*, 2016), geoacoustic inversion (Shi *et al.*, 2019; Dahl and Dall'Osto, 2020), and resolution of left/right ambiguity in towed passive acoustic arrays (Thode *et al.*, 2010a). They also have advantages when localizing signals, in that only two widely spatially separated sensors are required to successfully triangulate signals in a two-dimensional horizontal plane and without the need to be precisely time-aligned (Hawkes and Nehorai, 2003; Greene *et al.*, 2004).

Vector sensors also have key advantages when measuring directional properties of an ambient noise field. They can measure the field directionality over several octaves without suffering issues of ambiguities and spatial aliasing, such as beamforming sidelobes, that plague spatial arrays of hydrophones. As will be discussed Sec. II C vector sensor metrics also exist that provide insight into the second-order statistics, or angular distribution, of ambient noise sources.

This paper describes what are believed to be the first vector sensor measurements analyzing an arctic ambient noise field. The measurements were taken during late summer and early fall between 2008 and 2014 off the North Slope of Alaska, when no local ice fields are present. While ice presence is indeed a feature of the Arctic, which makes it unusual compared to most other ocean basins (Milne and Ganton, 1964; Diachok and Winokur, 1974; Makris and Dyer, 1991; Lewis, 1994; Uscinski and Wadhams, 1999; Stein *et al.*, 2000; Johannessen *et al.*, 2003), the open waters of the Arctic Ocean are fascinating in their own right because they remain, at present, areas without significant anthropogenic noise contributions from shipping at low

[a)]This paper is part of a special issue on Ocean Acoustics in the Changing Arctic.

[b)]Electronic mail: athode@ucsd.edu

[c)]ORCID: 0000-0001-7158-6852.

https://doi.org/10.1121/10.0006206

frequencies (Aulanier *et al.*, 2017; Halliday *et al.*, 2017; Ivanova *et al.*, 2020). In addition, the lack of long-distance swell eliminates most coastal surf noise (Wilson, Jr. *et al.*, 1985). Furthermore, bioacoustic activity can be less prominent than in other oceans, although song from bowhead whales and bearded seals can dominate the ambient noise field at certain times of year (Cummings and Holliday, 1987; Stafford *et al.*, 2008; Delarue *et al.*, 2009; Tervo *et al.*, 2011, MacIntyre *et al.*, 2013, Clark *et al.*, 2015). Consequently, wind-driven agitation of the ocean surface serves as the primary contributor to ambient noise along the North Slope, providing a rare window into a "simplified" ocean ambient environment where often the characteristics of only one principal sound source need be considered when interpreting results. Here, we show that this simplified ocean displays a precise and consistent long-term directionality under certain easily measured circumstances, which suggests that this noise directionality is a persistent feature of the Alaskan North Slope.

After Sec. II defines the vector sensor metrics used to characterize ambient noise levels and their angular distribution, Sec. III describes the equipment, deployment, and analysis methods. Section IV covers the results over increasingly larger time scales, and Sec. V discusses the implications of the existence of this consistent long-term feature.

II. THEORY

A. Active and reactive intensity

The intensity of an acoustic field is the product of its acoustic pressure and particle velocity. Conventional hydrophones can only measure acoustic pressure, so most ambient noise studies assume that the particle velocity is proportional to and in phase with the acoustic pressure and thus, the squared acoustic pressure can represent the true underlying intensity. These assumptions are valid in the restricted case of plane waves arriving from a distant, dominant, and spatially compact source. However, in many circumstances, the particle velocity is not proportional to or in phase with the acoustic pressure, so the squared sound pressure is proportional only to the signal's potential acoustic energy density, and not its intensity. In contrast to conventional hydrophones, acoustic vector sensors can provide direct measurements of the acoustic intensity, due to their ability to measure particle velocity independently from acoustic pressure.

The vector sensors discussed in this paper are two-dimensional, measuring particle velocity $v_x(t)$ and $v_y(t)$ along two orthogonal horizontal axes and acoustic pressure $p(t)$. Thus, the vertical component of velocity shall be (mostly) ignored here. Each of the three time series can be converted into a time-frequency representation using the short-time Fast Fourier Transform (FFT), where each time-frequency bin at sample time T and frequency f is represented by complex coefficients $p(f,T)$, $v_x(f,T)$, and $v_y(f,T)$. The time-averaged complex acoustic intensity $\tilde{I}_k$ along a given axis k (Mann III *et al.*, 1987; D'Spain *et al.*, 1991; D'Spain *et al.*, 2006; Dall'Osto *et al.*, 2012) can then be determined from

$$\tilde{I}_k(f,T) = \langle p(f,T)v_k^*(f,T)\rangle \equiv I_k(f,T) + iQ_k(f,T) \quad (1)$$

where the symbol "*" indicates a complex conjugate, the operator $\langle\ \rangle$ designates either an ensemble average or a time average of a statistically stationary random acoustic field, and I_k and Q_k, both real numbers, represent the active and reactive components, respectively, of the acoustic intensity along axis k. Equation (1) can be applied to each particle velocity axis to define vector quantities for active and reactive intensity. When processing stochastic signals, the variance of Eq. (1) can be reduced by averaging samples over a short time window, just as a periodogram averages Fourier Transform snapshots to reduce their variance (Oppenheim and Schafer, 1989).

The active intensity comprises the components of pressure and particle velocity that are in phase. It is proportional to the phase gradient of the acoustic field, indicating the portion of that field that is transporting acoustic energy through the measurement point. The reactive intensity, which incorporates the quadrature components of p and v_k, is proportional to the pressure gradient of the field, indicating the portion of that field that is maintaining the spatial heterogeneity in acoustic pressure magnitude. Although originally defined for monochromatic acoustic fields (Mann III *et al.*, 1987), the concepts of active and reactive intensity have been extended into more broadband fields as well (Schiffrer and Stanzial, 1994). For the case of a lossless shallow waveguide, where the acoustic field can be represented by a set of normal modes, the vertical component $\tilde{I}_z$ is theoretically imaginary, and thus the active intensity vector is horizontal. In a real ocean a vertical component of the active intensity does exist, due to the transmission of acoustic energy into the sea floor. In a deep-water environment, this vertical active intensity component can become an important component of the acoustic field (D'Spain *et al.*, 1991), but its contributions will be mostly neglected here.

The relative contributions of the active and reactive intensity to the total intensity are conveniently expressed by the intensity phase γ:

$$\gamma(f,T) = \tan^{-1}\left[\left\langle\sqrt{Q_x^2+Q_y^2}\right\rangle \Big/ \left\langle\sqrt{I_x^2+I_y^2}\right\rangle\right]. \quad (2)$$

A value of 0° indicates the field is completely active; a value of 90° is completely reactive. For the case of a pulsating spherical source, the intensity phase falls below 10° at ranges greater than an acoustic wavelength (Kinsler *et al.*, 1982)—a fact that is exploited in Sec. III C when calibrating the sensors.

B. Dominant azimuth

Several metrics can be derived from the active and reactive intensity. The dominant azimuth φ associated with a

noise field relative to the y coordinate (North) at time T and frequency f can be inferred from the relative magnitudes of the active acoustic intensity along each measurement axis:

$$\varphi(f,T) = \tan^{-1}\left[I_x(f,T)/I_y(f,T)\right]. \tag{3}$$

The use of the form $\tan^{-1}$(x/y), as opposed to $\tan^{-1}$(y/x), produces an azimuth that follows the geographic convention (φ increasing clockwise from the y axis) instead of the mathematical convention (φ increasing counterclockwise from the x axis). Equation (3) can be plotted as an image with respect to time and frequency in a manner similar to a spectrogram (Thode *et al.*, 2019). In all the examples that follow, the dominant azimuth will be defined in terms of where acoustic energy is propagating toward, as opposed to the direction energy is propagating from, in order to avoid discontinuities between 0 and 360° when plotting images of the directionality.

C. Velocity of acoustic energy transport

Equation (3) indicates the dominant azimuth from which acoustic energy is being transported but provides no information about the azimuthal arrangement of acoustic sources that produces this result. Various measures of the magnitude of the active intensity vector provide additional insight into the source distributions.

The active intensity magnitude can be normalized for a 2-D vector sensor by taking the ratio of the magnitude of acoustic intensity to the energy density of the field at that point (Mann III *et al.*, 1987; D'Spain *et al.*, 1991):

$$\hat{U}_c = \frac{\left\langle \sqrt{I_x^2 + I_y^2} \right\rangle}{\frac{1}{2}\rho_0 \left\langle \left(v_x^2 + v_y^2\right) \right\rangle + \left(\frac{1}{2\rho_0 c^2}\right)\langle p^2 \rangle} \tag{4a}$$

$$U_c \equiv \frac{\hat{U}_c}{c}, \tag{4b}$$

where ρ_0 and c are the propagation medium density and sound speed. The denominator of Eq. (4a) is the sum of the acoustic kinetic energy density (proportional to the square magnitude of the particle velocity vector) and the acoustic potential energy density (proportional to the square magnitude of the acoustic pressure). The quantity $\hat{U}_c$ [Eq. (4a)] has been dubbed "net velocity of acoustic energy density transport" (D'Spain *et al.*, 1991) and "the velocity of energy transferred by the average intensity" (Schiffrer and Stanzial, 1994). $\hat{U}_c$ has units of velocity and can reach a maximum value equivalent to the medium sound speed $2c/(1+\sec\theta)$. θ is the vertical elevation angle $\tan^{-1}\left(\langle I_z\rangle / \left\langle \sqrt{I_x^2 + I_y^2} \right\rangle\right)$ of the dominant propagating field; e.g., the grazing angle of the dominant modes(s).

When this velocity is normalized by the medium sound speed c (set to be 1470 m/s here, based on historical water temperature data), the resulting quantity U_c [Eq. (4b)] is defined here as the "normalized energy density transport velocity", or simply "transport velocity," with possible values between 0 and $2/(1+\sec\theta)$, where the latter approaches one when most of the acoustic energy is propagating nearly horizontally, as is the case for energy arriving from distant low-frequency sources in a shallow waveguide.

The physical interpretation of Eq. (4) is that it measures the net speed that the time-averaged energy is being transported through a point. The transport velocity depends on both the density and sound speed of the medium at the measurement point, but does not depend on these properties outside the point (e.g., a sound speed profile). As a practical interpretation, the normalized transport velocity provides insight into the azimuthal distribution of the sources generating the field, provided that the energy from the sources is mostly propagating horizontally. Consider two extreme cases. In case one, a maximum transport velocity of one indicates a field with pressure and particle velocity completely in phase, no reactive intensity, and equal values of kinetic and potential energy density (Schiffrer and Stanzial, 1994). This situation may arise when an azimuthally compact acoustic source, such as a ship or whale, generates a high source level sound from a sufficient distance such that the signal's wavefront curvature at the receiver is negligible, while still maintaining a high signal-to-noise ratio to reduce interference from other sources. Under these circumstances, both the acoustic intensity and energy density of the transient field are completely dominated by this horizontally propagating signal, and all signal energy propagates at the medium's speed of sound. In case two, at the other extreme, a transport velocity of zero indicates that pressure and particle velocity are 90° out of phase (in quadrature), the active intensity is zero, and no net energy is being transported through the measurement point. Such a situation occurs with a standing wave, when two-plane waves of equal amplitude, $Ae^{i(kx-\omega t)}$ and $Ae^{i(-kx-\omega t)}$, propagate in opposite directions through a point, with k being the medium wavenumber, ω being the radial frequency, and x a one-dimensional coordinate. The interference between the waves produces an acoustic pressure of $2A\cos(kx-\omega t)$ and particle velocity of $-2A\sin(kx-\omega t)/\rho c$. Since the resulting pressure and particle velocity are 90° out of phase, the complex time-averaged acoustic intensity pv^* is completely reactive, i.e., $-i2A^2\sin(2kx)/\rho c$, and the normalized transport velocity becomes zero. No net energy is transported through the point because energy is propagating from two opposite directions; the azimuthal distribution of sources is extremely "broad" in the sense that the two sources are separated by 180°. Therefore, one interpretation of a low transport velocity is that multiple distant acoustic sources are distributed over a wide angular distribution, such that the net transport of energy across the measurement location is lower than hydrophone measurements of acoustic pressure alone would indicate.

These examples indicate that transport velocity can be a useful metric for characterizing the angular spatial distribution of a collection of acoustic sources. If an ambient noise

https://doi.org/10.1121/10.0006206

field is envisioned as the sum of numerous azimuthally distributed sources, then a low transport velocity would indicate a relatively non-directional ambient sound field, while a high transport velocity would indicate strong directionality. The transport velocity can also be interpreted as a measure of azimuth asymmetry in an ambient source distribution. These interpretations are only valid on a 2-D vector sensor for situations where energy is arriving mostly from the horizontal.

Both the normalized transport velocity [Eq. (4b)] and the intensity phase [Eq. (2)] are highly correlated, as both are measures of the relative contributions of the active and reactive intensity to the complete intensity vector.

D. Ratio of kinetic to potential energy

A final metric is the ratio of the kinetic to potential energy of the ambient field, K/P:

$$K/P = \frac{\frac{1}{2}\rho_0\left\langle\left(v_x^2 + v_y^2\right)\right\rangle}{\left(\frac{1}{2\rho_0 c^2}\right)\langle p^2\rangle}. \tag{5}$$

Here, the K/P ratio is used as a quality diagnostic: a ratio much greater than one (i.e., particle velocity is very large, while pressure is very small) is a sign of non-acoustic mechanical vibration contamination on the sensor. Measurements of the K/P ratio were used to identify a lower frequency bound of 20 Hz in the measurements; frequencies below that bound were susceptible to vibrations from flow noise.

III. METHODS

A. Equipment and deployment

Between 2007 and 2014, Shell Exploration and Production Company (SEPCO) commissioned Greeneridge Sciences, Inc. to deploy and build at least 35 Directional Autonomous Seafloor Acoustic Recorders (DASARs), divided among five sites over a 280 km swath in the coastal Beaufort Sea. With a few exceptions, the DASARs were only deployed between August and October of each year in mostly ice-free conditions to monitor the fall migration of the Chukchi–Beaufort bowhead whale population. DASARs (model C) are autonomous acoustic recording packages equipped with an omnidirectional acoustic pressure sensor (–149 dB re 1 μPa/V @ 100 Hz) and two horizontal directional sensors capable of measuring the north–south and east–west components of acoustic particle velocity (Greene *et al.*, 2004; Thode *et al.*, 2016). The signals measured on each of the three channels were sampled at 1 kHz and have a maximum measurable acoustic frequency of 450 Hz. The sensitivity of the directional channels, when expressed in terms of plane wave acoustic pressure (–243.5 dB re m/s equates to 0 dB re 1 μPa), is −146 dB re 1 μPa/V @ 100 Hz. The sensitivity of all channels increases by +6 dB/octave (e.g., the sensitivity of the omnidirectional channel is −140 dB re 1 μPa/V @ 200 Hz), since the channel inputs are differentiated before being recorded. These values were measured from two DASARs calibrated at the U.S. Navy's underwater acoustic test facility TRANSDEC in San Diego in 2008. A finite impulse response (FIR) equalization filter was applied to recorded data to recover the original spectrum.

The noise floor of the omni channel is 43 dB re 1 μPa ^{2}/Hz @ 100 Hz and decreases 6 dB per octave (Fig. 1). It was measured *in situ* during an under-ice overwinter mission, using the 0% percentile curve, and is well below the Knudsen Sea State Zero curve. While not directly measured, the noise floor of the particle velocity channels is roughly 6 dB greater at the same frequency, when expressed in terms of pressure. The DASAR electronics saturate whenever the peak sound pressure exceeds 151 dB re 1 μPa @ 100 Hz.

At each site, DASARs were deployed on the ocean floor in triangular grids with a typical separation of 7 km (Fig. 2). They were installed with no surface expression, which is important to avoid entanglement with ice floes. One corner of the DASAR frame was attached with a shackle to 110 m (360 ft) of ground line, which ended with 1.5 m (5 ft) of chain and a small anchor.

The southernmost DASAR at a site is labeled "A", with letters increasing alphabetically to DASAR "G" at the northernmost (and usually deepest) location. Each individual DASAR is referenced via site number and letter; e.g., DASAR 5 G refers to the northernmost DASAR at Site 5 (Fig. 2). The depth across all sites varied between 20 m and 53 m, with DASAR G, the baseline sensor for this study, being one of the deeper sensors.

The original motivation of the DASAR deployments was to evaluate the potential impact of airgun and other industrial sounds on bowhead whale behavior during their westward fall migration (Blackwell *et al.*, 2015; Thode *et al.*, 2020). In addition, these data have previously been

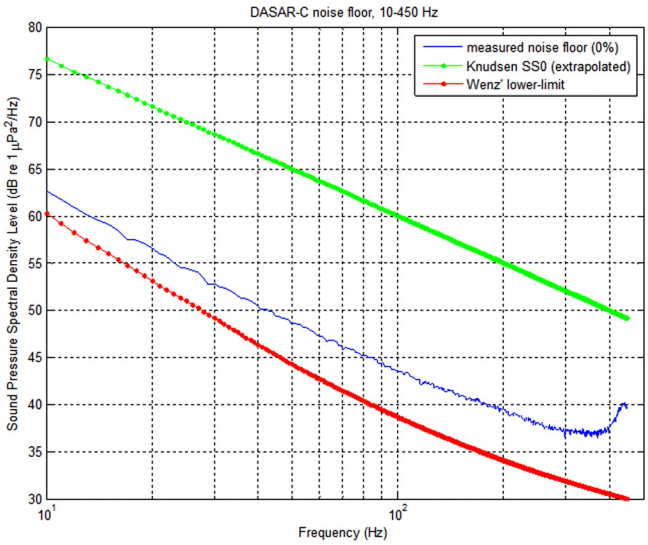

FIG. 1. (Color online) Noise floor of DASAR-C, measured during overwinter conditions, 0% percentile level.

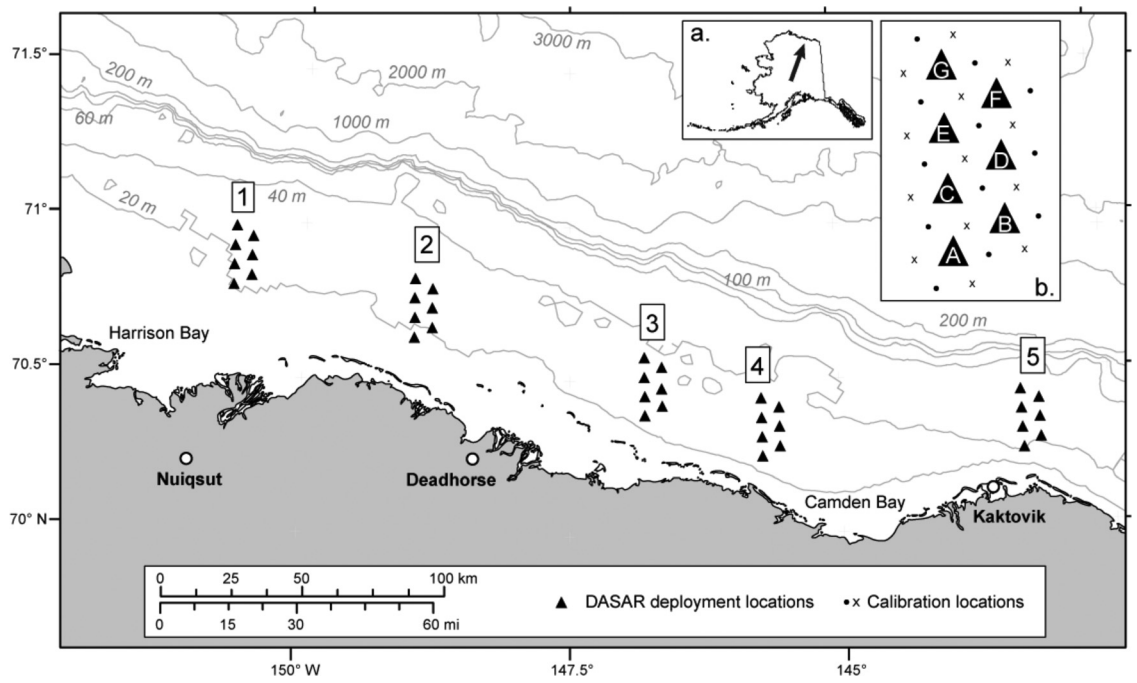

FIG. 2. Location of 35 DASAR sensors on the Alaskan North Slope, deployed during open-water conditions (August–October) over seven consecutive years. Boxed numbers are site numbers. Inset (b) shows how DASARs within a site are labeled, along with calibration locations. DASAR G at Site 5 (5 G) is the baseline instrument used in this study.

used to track distant seismic sources (Thode *et al.*, 2010b), characterize seismic survey reverberation (Guerra *et al.*, 2011), and demonstrate how vector sensors can null out directional industrial noise sources (Thode *et al.*, 2016).

B. *In situ* calibration of DASAR orientation

When DASARs are lowered to the seafloor, their orientation with respect to true north is unknown. In addition, each DASAR contains a clock that has a small but significant drift, which must be compensated for throughout the course of the deployment period (Greene *et al.*, 2004). Field calibrations for time and bearing consisted of transmitting test sounds underwater at known times and known locations from a deployment vessel and recording these sounds on the DASARs [shown as dots and x's in Fig. 2(b), inset]. The data from these transmissions were then post-processed to determine each DASAR's orientation on the seafloor. During the first few years of the project, calibration transmissions were projected at six locations around each DASAR, at a distance of about 4 km. During later years, transmissions were projected at three locations (dots in inset).

Equipment used for calibrations included a J-9 sound projector (Naval Undersea Warfare Center, Newport, RI), an amplifier, a computer to generate the projected waveform, and a GPS receiver to control the timing of the sound source and determine its position. Two different waveforms were projected. The first consisted of a 2 s tone at 400 Hz, a 2 s linear sweep from 400 to 200 Hz, a 2 s linear sweep from 200 to 400 Hz, and a 2 s linear sweep from 400 to 200 Hz. The second waveform consisted of the same 8 s as described for the first waveform, but with an added 4 s long section of pseudo-random noise, i.e., an m-sequence with 255 chips, repeated once every second and on a 255 Hz carrier frequency. The source level of both of these waveforms was ~150 dB re 1 μPa @ 1 m. During calibration, a waveform transmission was initiated every 15 s, for a total duration of about 2 min (i.e., eight to nine transmissions). Calibration of one entire site took 6–7 h. Each site was calibrated directly following the deployment of its DASARs, and again immediately prior to DASAR retrievals. The result of each calibration was (i) a "reference azimuth" for each DASAR which was subsequently added to future raw azimuth estimates to generate an azimuth referenced to true north, and (ii) an approximation of time offset and drift.

The random orientations of the sensors on the ocean floor were convenient in the sense that they helped confirm that any directional effects observed in the ambient sound field did not arise from self-noise or miscalibrated particle velocity channels.

C. *In situ* phase calibration between pressure and particle velocity

A proper phase calibration between the pressure and particle velocity channels is essential for determining the active and reactive components of acoustic intensity. However, DASARs were originally designed to track bowhead whale calls, whose peak frequency rarely exceeds 200 Hz during the fall migration. As a result, while the relative phase between the three channels was calibrated below 200 Hz, the phase between the pressure and particle velocity channels between 200 and 500 Hz had not been calibrated

https://doi.org/10.1121/10.0006206

during the historical deployments. Fortunately, a few hours after a DASAR deployment, the ship would return near the deployment location and drift for several minutes to allow a transponder to interrogate the package to confirm operation. When the ship reengaged its propellor, it generated a burst of broadband cavitation noise whose power spectral density exceeded 100 dB re 1 μPa^2/Hz between 100 and 450 Hz for nearly 30 s. The range of the ship from the DASAR was always beyond 150 m, sufficient to ensure an intensity phase of less than 10° for frequencies above 10 Hz, since the vessel was greater than an acoustic wavelength away from the sensor. This assumption of an intensity phase of less than 10° provided a calibration reference. We averaged 20 s of data from DASAR 5 G on 17 August 2014 00:06:30 LT (local time) in order to derive the phase shift, averaging a total of 153 256-pt FFTs. The result was a linear phase correction versus frequency, which was subsequently compared to other high-cavitation events, such as during the DASAR 5 G retrieval on 1 October 2014 23:57:28 LT as well as during a different DASAR instrument's retrieval at the same 5 G location but 4 yrs earlier on 04 October 2010 02:45:47. The resulting intensity phase between the two instruments and two deployments varied by less than 10° up to 375 Hz. Spot checks of the intensity phase for high-SNR seismic airgun signals and bowhead whale harmonics above 200 Hz also yielded intensity phases of 5° or less, supporting the validity of this approach.

D. Bulk signal processing

The entire DASAR record was processed in bulk by loading the three-channel data, passing it through the Finite Impulse Response (FIR) equalization filter, and conducting a set of 256-point Fast Fourier Transforms (FFTs), overlapped by 75%. The complex time-averaged acoustic intensity was computed from Eq. (1) after averaging 15 FFT snapshots over 1 s. The acoustic potential and kinetic energy densities in the denominator of Eq. (4) were also averaged in identical fashion. Averaging the data over intervals greater than 1 s only had a minor influence on the results.

Every minute, the joint distributions of the metrics defined in Eqs. (2)–(4) were computed as a function of frequency between 20 and 475 Hz, along with the hydrophone pressure power spectral density (PSD) typically used for ambient sound level estimates. Azimuths were binned in 2° increments, phase intensities in 2° increments, normalized transport velocities in (unitless) 0.02 increments, and PSD estimates in 1 dB increments between 40 and 110 dB re 1 uPa^2/Hz. All measurements were binned in 4 Hz frequency increments. From these joint distributions, one could then derive marginal and conditional distributions.

IV. RESULTS

A. Time series example: Site G, 2014

Figure 3 displays the time evolution of the dominant azimuth [Eq. (3); subplots a, e], PSD (subplots b, f), normalized transport velocity U_c [Eq. (4b); subplots c, g], and intensity phase [Eq. (2); subplots d, h] of the ambient sound field at two frequencies (100 Hz and 350 Hz) over five days of a deployment at a 52 m depth at DASAR 5 G during 2014, the final year of the project. Relatively little seismic exploration activity occurred during that year, providing a window into the dynamics of the undisturbed natural ambient sound properties under open-water conditions. As discussed in Sec. II B, the dominant azimuth is displayed in terms of the direction acoustic energy is propagating *toward*,

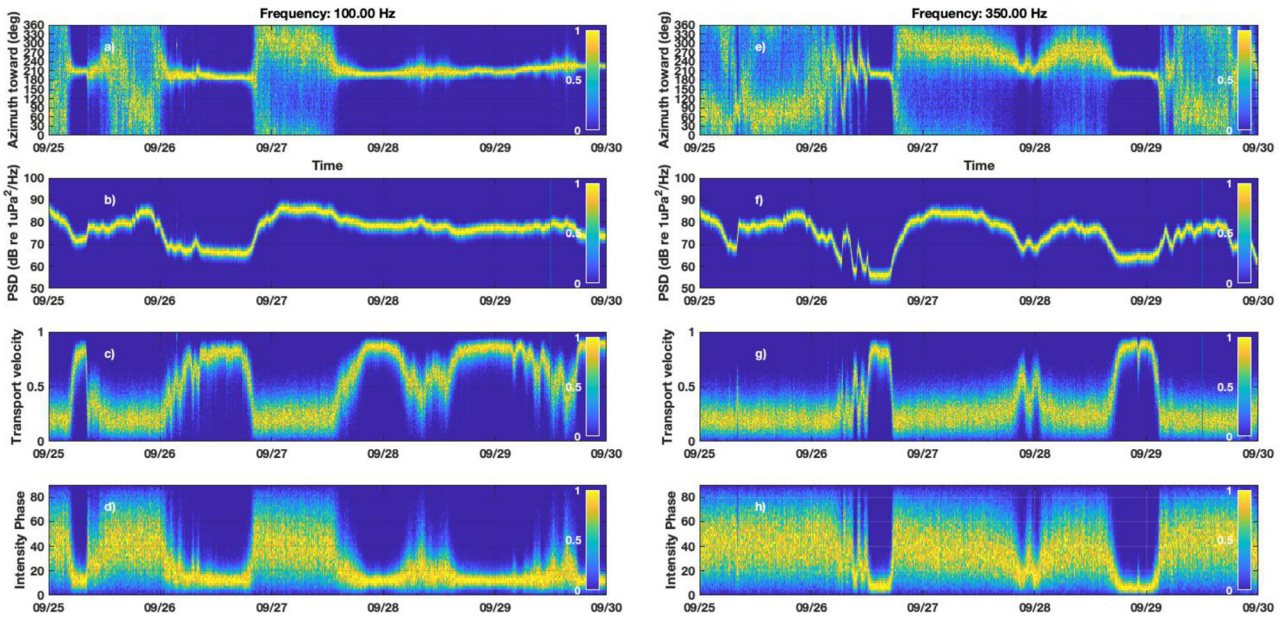

FIG. 3. (Color online) Distributions of dominant azimuth [Eq. (3); subplots a, e], pressure power spectral density (PSD) (subplots b, f), normalized transport velocity [Eq. (4b); subplots c, g] and intensity phase in degrees [Eq. (2); subplots d, h], with 1 s averaging and distributions computed over 5 min intervals across five days (9/25–9/30) at DASAR 5 G in 2014. Each 5 min distribution has been normalized by its maximum value (mode of the conditional probability distribution). Left column: 100 Hz; Right column: 350 Hz.

not the direction from which it is arriving. Thus, in Fig. 3, the dominant azimuth plot is showing that acoustic energy at 100 Hz is often propagating from a geographic azimuth of 30° (NNE) toward 210° (SSW).

The intensity phase (subplots d, h) shows a clear relationship with U_c (subplots c, g): during times of high transport velocity, the phase is near 0°, but during times when the transport velocity is relatively low, the phase distribution is centered around 45°, suggesting that the horizontally propagating field is equally partitioned between active and reactive components.

Theoretical models of both an isotropic and completely azimuthally symmetric wind-driven noise field predict that the active intensity should be zero and the intensity phase undefined (Deal, 2018). As a consequence, the field measured in this environment cannot be fully azimuthally symmetric, even under low-directionality (and low U_c) conditions, but no theoretical explanation exists for why the phase should be distributed around 45°.

B. Correlation between azimuth and other metrics, all season 2014

Figure 4 provides an expanded view into how the ambient sound directionality at the two frequencies is correlated with various metrics, using all days monitored during the 2014 deployment of DASAR 5 G. Each row of every image in Fig. 4 displays the cumulative conditional distribution of the dominant azimuth, conditioned on the metric plotted on the x axis, $p(Azimuth|metric)$. As stated in Sec. III D, every data point used to compute these distributions was computed from 1 s (15 FFT) averaged data samples.

Although both the PSD and normalized transport velocity U_c are measurements of ambient sound field magnitude, Figs. 3, 4(a), and 4(d) suggest that the correlation between the two is not straightforward. To clarify this relationship, Figs. 5 and 6 plot the cumulative distribution of U_c, conditioned on PSD, $p(U_c|PSD)$, at 100 Hz and 350 Hz, for three DASARs at Site 5 across two different deployment years (2014 in Fig. 5 and 2010 in Fig. 6). As will be discussed in Sec. V A, two distinct regimes exist in the diffuse ambient sound field.

C. Dominant azimuth across entire bandwidth

Figures 7 and 8 display statistics relating to the ambient sound field's dominant azimuth [Eq. (3)], measured across the entire recording bandwidth for the 2014 and 2010 seasons, respectively. For a given frequency, all 1 s averaged measurements were subdivided by their U_c values into bins incremented by quantities of 0.01. The circular median was then computed from the dominant azimuths associated with each transport velocity bin, along with the circular interquartile range (IQR) as a measure of the spread of the azimuthal estimates. Figures 7 and 8 contour-plot the resulting median azimuths (left column) and IQR (right column) as a function of frequency and U_c at the same three Site 5 locations analyzed in Figs. 5 and 6. Figure 9 conducts a similar analysis for 2014 at a different location, Site 3, on DASARS B, D, and G. (DASARs B and D were used instead of A and C at this site because they recorded successfully across all deployment seasons.)

V. DISCUSSION

A. Normalized transport velocity defines distinct ambient sound regimes

Although it only displays five days of data, Fig. 3 illustrates some key features of the arctic open-water ambient sound field that persist across multiple seasons and locations. Figures 3(b) and 3(f) show that within any given 5 min interval, the ambient noise levels (in terms of PSD at a particular frequency) are stationary, yielding estimates with standard deviations less than 3 dB. Across the five days; however, the same figures show the mean PSD can shift by over 20 dB. Throughout the five days, the dominant directionality switches between two states (subplots a, e): a relatively nondirectional state [e.g., Fig. 3(a)], for 100 Hz between noon on September 25, 2014, and midnight on September 26, 2014; between midnight and noon 9/27) and a highly directional state with energy propagating toward 210° [e.g., Fig. 3(a) after September 28, 2014]. These distinct directional states seem relatively uncorrelated with omnidirectional sound pressure level measurements; for example, for PSD levels of 68 dB re 1 $\mu Pa^2/Hz$, the 100 Hz field can be in either directionality state [Fig. 3(b)]. Over the five days, the 100 Hz ambient sound field is more likely to exist in a directional state than the 350 Hz field.

By contrast, measurements of the normalized transport velocity and intensity phase (subplots c, d, g, h) are highly correlated with distribution of the dominant azimuth: the higher the transport velocity and the lower the intensity phase, the tighter and more directional the azimuthal distribution. This is not surprising, given the interpretation of transport velocity reviewed in Sec. II C. Figure 4 confirms that the ambient field becomes steadily more directional as the normalized transport velocity increases, with a sharp decrease in the dominant azimuth distribution's spread as U_c transitions between 0.5 and 0.6 at both frequencies [Figs. 4(b) and 4(e)].

The relationship between the dominant azimuthal distribution and PSD [Figs. 4(a) and 4(d)] yields little insight, but contouring the distribution of U_c against PSD (Figs. 5 and 6) across two different field seasons yields a robust relationship between the two metrics. Distinct regimes are visible across Site 5. At high spectral density levels (PSD exceeding 88 dB re 1 uPa^2/Hz) all transport velocity measurements are uniformly clustered near one. These data represent discrete high-SNR transient signals arising from spatially compact sources, such as airguns or whale calls, and are not truly part of the diffuse ambient sound regime.

The first regime associated with ambient sound occurs at slightly lower PSD levels, where the transport velocity drops below 0.5, with a median around 0.2, resulting in an ambient sound field that is only weakly directional (large

https://doi.org/10.1121/10.0006206

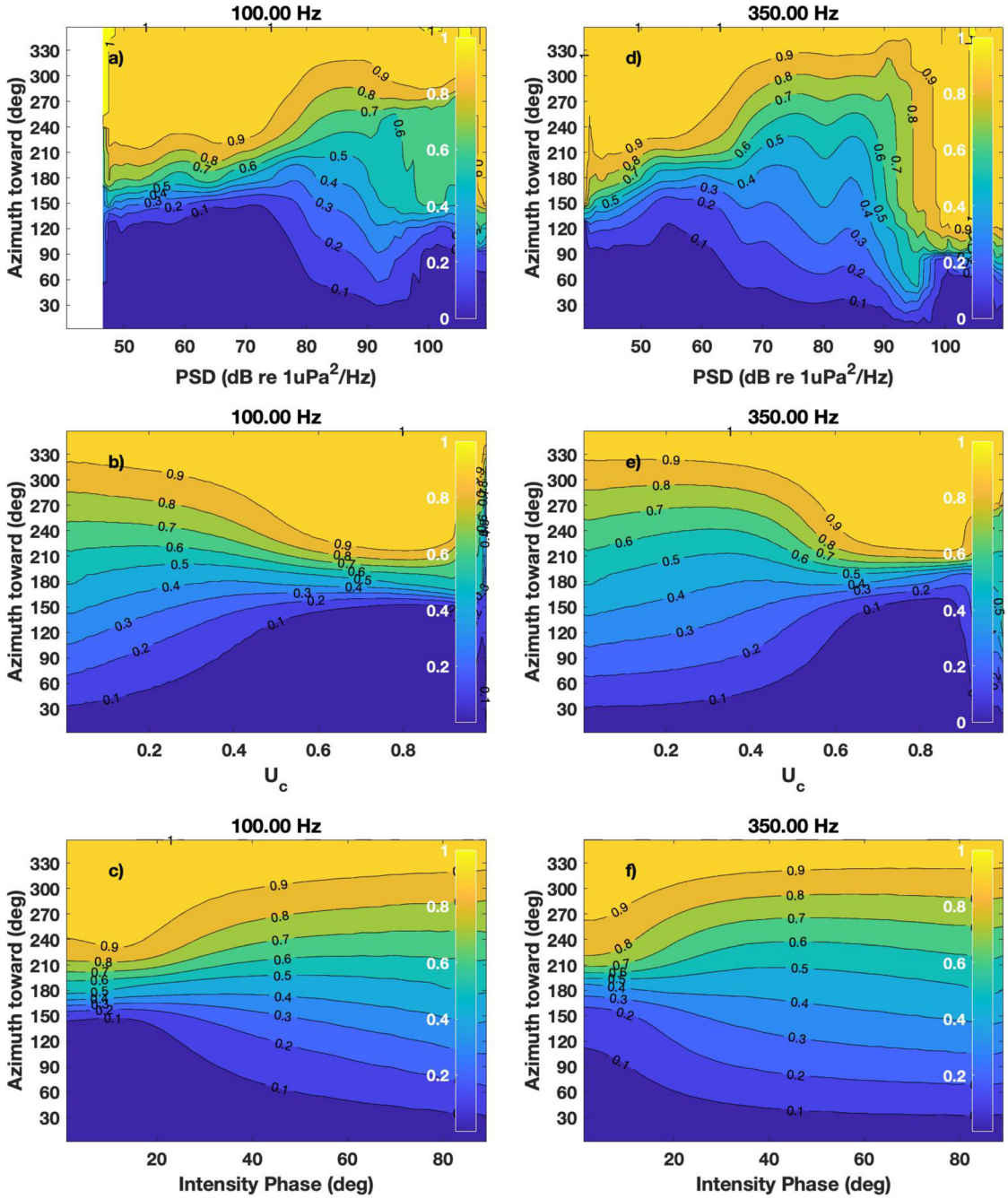

FIG. 4. (Color online) Cumulative distributions of conditional probability of dominant azimuth $p(Azimuth|metric)$ for various intensity metrics, derived from data accumulated on DASAR 5 G between 8/16/2014 and 10/01/2014. The left column shows 100 Hz, the right column 350 Hz. Each column shows the cumulative distribution of the dominant azimuth, given (a and d) power spectral density, (b and e) normalized transport velocity U_c, and (c and f) intensity phase. The blank region in a) exists to permit the x axes of the 100 Hz and 350 Hz data to be displayed over the same timescale (no PSD values at 100 Hz fell below 48 dB).

spread in the dominant azimuthal distribution). This region of relatively high PSD but low transport velocity, occurs over a much broader spread of PSD values at 350 Hz than at 100 Hz, but the resulting conditional distributions of transport velocity are similar between the frequencies. This regime is interpreted as arising from the presence of local storms that agitate the ocean surface over a wide azimuthal swath surrounding the instrument. Figures 3(a) and 3(e) show that any weak directionality in this regime tends to migrate over time, although at any given instant, the dominant azimuth between the two frequencies often differs. The transport velocity may also have lower values in this regime because a higher proportion of the acoustic field is arriving from the near field, and thus, from larger grazing angles, reducing the maximum value that U_c can obtain $[2/(1+\sec\theta)]$.

The second ambient sound regime occurs in the lower measured range of the standard PSD measurements, when

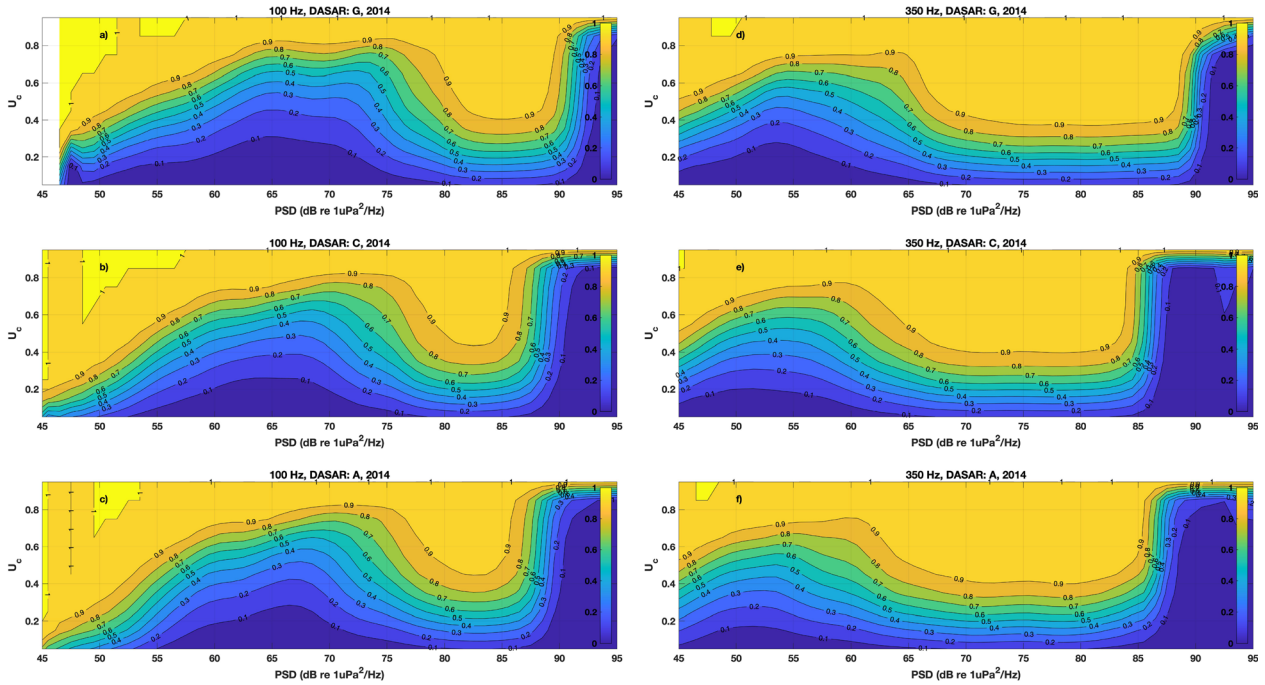

FIG. 5. (Color online) Normalized transport velocity (U_c) cumulative distribution, conditioned on pressure power spectral density $p(U_c|PSD)$, computed over the same time interval in 2014 as Fig. 4. Left column: 100 Hz; Right column: 350 Hz. Top row (a, d): DASAR 5 G (52 m depth); Middle row (b, e): DASAR 5 °C (53 m depth); Bottom row (c, f): DASAR 5 A (39 m depth).

the normalized transport velocity distribution shifts to higher levels, with the median value of U_c exceeding 0.5. This transition away from relatively low transport velocity occurs at 76 dB re 1 μPa ^{2}/Hz @ 100 Hz [e.g., Fig. 5(a)] and 65 dB @ 350 Hz [e.g., Fig. 5(b)]. This regime, which roughly lies between PSD levels of 52 and 78 dB in Fig. 5(a), exists in 55% of the deployment's 100 Hz data samples and 32% of the deployment's 350 Hz data samples. At extremely low ambient sound levels below 55 dB, the transport velocity does decrease to levels consistent with nondirectional distributions, but these data are relatively rare, comprising less than 1.1% of the total samples in Fig. 5(a), and so, this situation is not discussed further here.

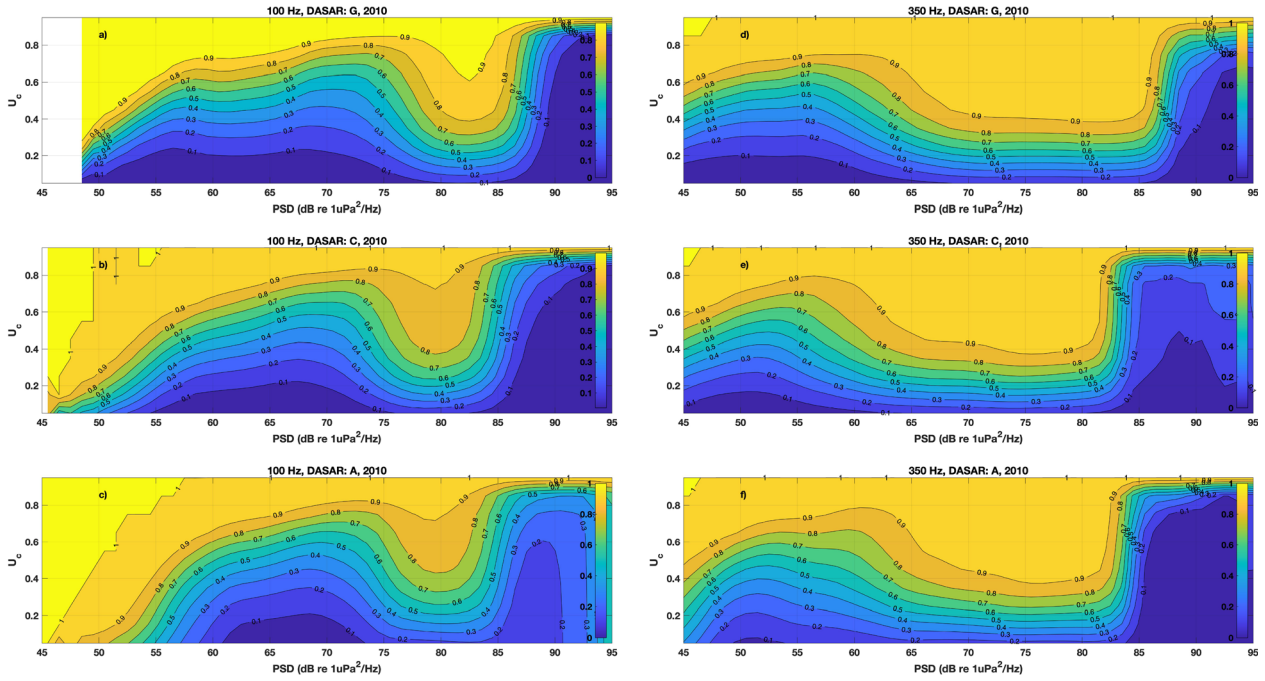

FIG. 6. (Color online) Same as Fig. 5, expect using data from the entire 2010 deployment.

https://doi.org/10.1121/10.0006206

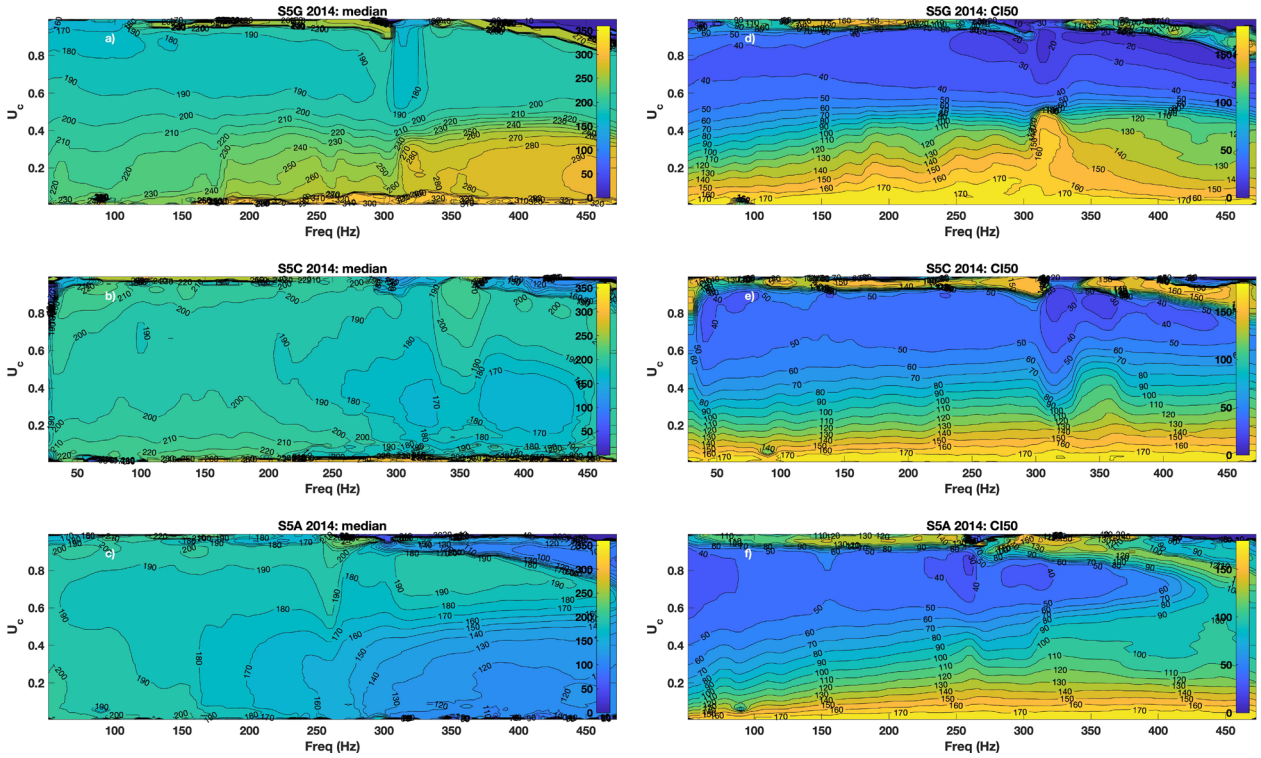

FIG. 7. (Color online) Left column: contour plot of circular median of dominant azimuth as a function of frequency and normalized transport velocity U_c, at Site 5 in 2014. Right column: circular inter-quartile range (IQR) of the azimuthal estimate. Top, middle, and bottom rows display DASARs G, C, and A, respectively. In all plots, colors represent angle in degrees.

A high transport velocity at lower PSD values indicates a field with a more spatially asymmetric source distribution, which results in the narrow azimuthal distribution visible throughout Figs. 3(a) and 3(e). Because the PSD bounds on each regime vary with frequency, a highly directional field can exist at 100 Hz while at 350 Hz it is non-directional, even when both frequency components have similar PSD values [e.g., Figs. 3(a) and 3(e) at noon on September 29, 2014). A

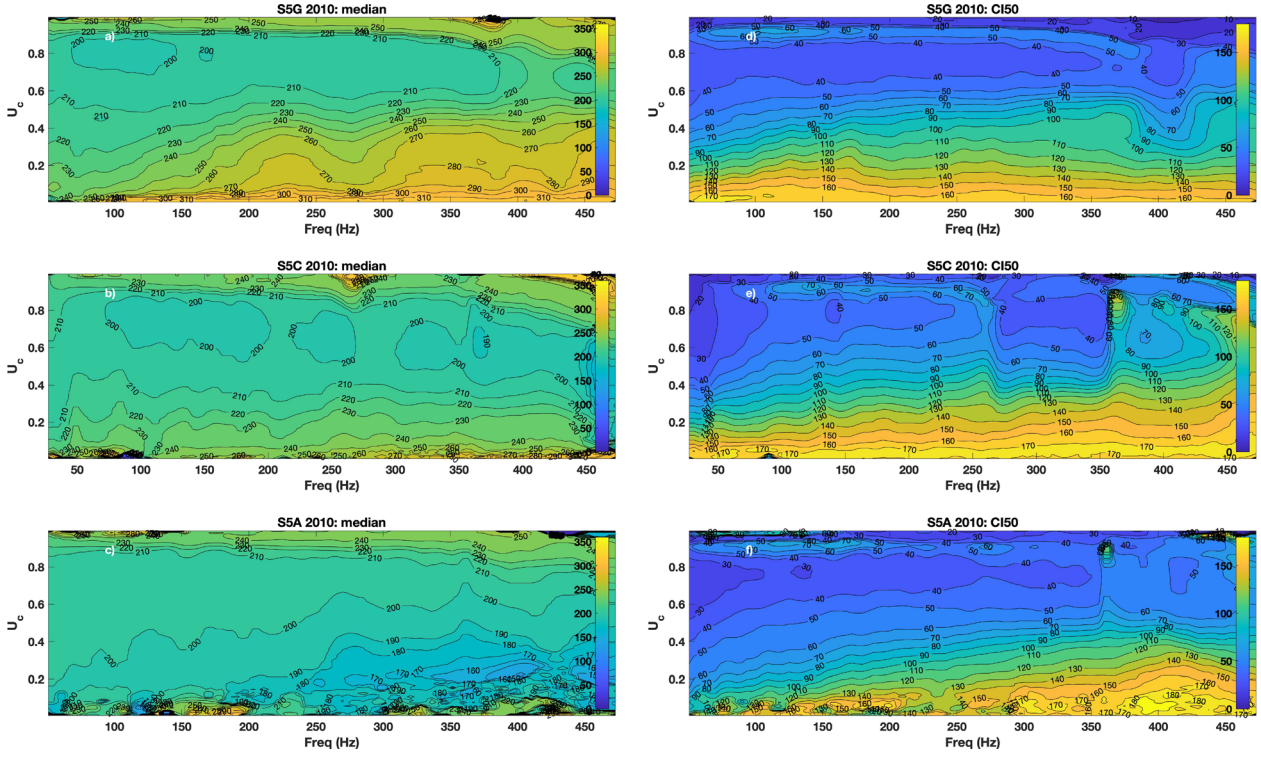

FIG. 8. (Color online) Same as Fig. 7, but for the 2010 deployment.

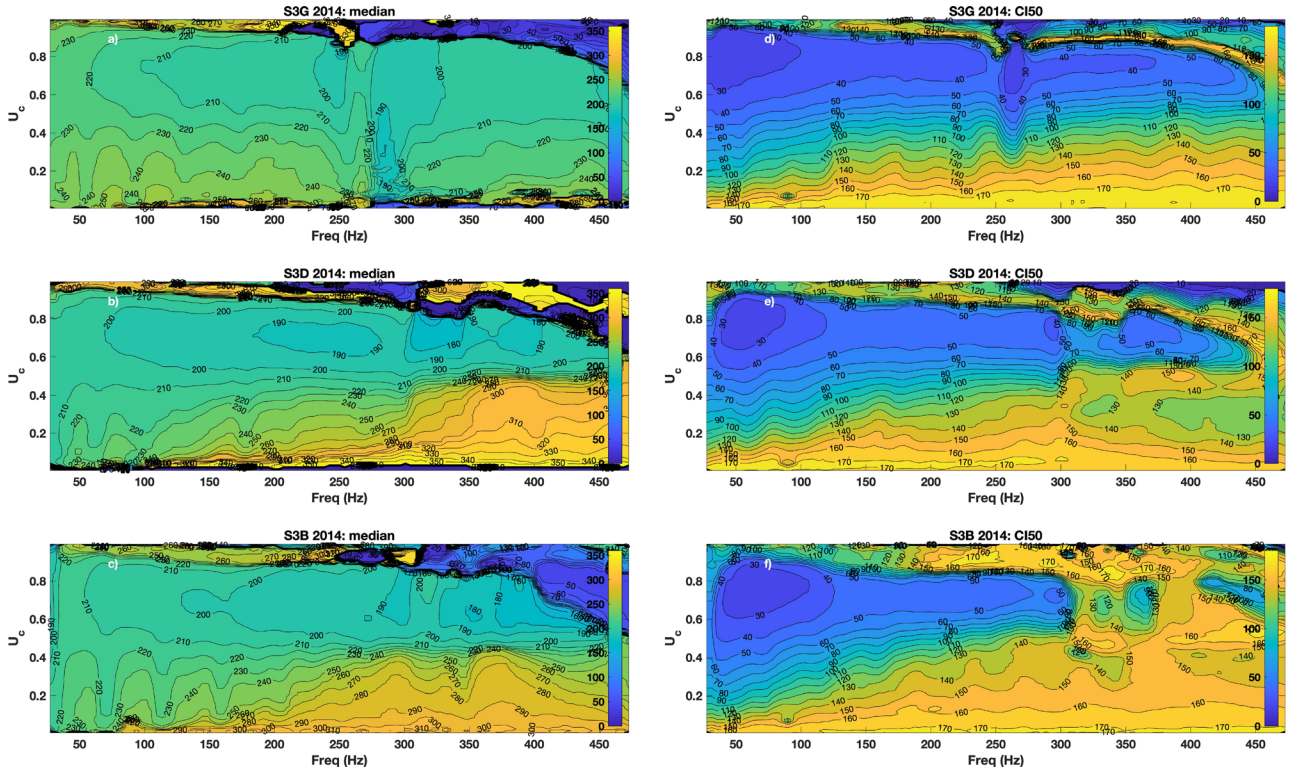

FIG. 9. (Color online) Circular median and IQR of dominant azimuth at Site 3 in 2014. Top, middle, and bottom rows display statistics from DASARs G (39 m), D (38 m), and B (34 m).

conventional spectrogram of the ambient noise field under these circumstances would thus provide no indication of the difference in directionality between the two frequencies.

The transition between these regimes can occur over a relatively narrow change in ambient PSD. For example, at 100 Hz, the switch from a low to high transport velocity occurs over a 6 dB PSD window [Figs. 5(a)–5(c)], across an ambient noise field with a dynamic range of over 40 dB. The transition between states is more gradual for the 350 Hz signal [Figs. 5(d)–5(f)]. Figure 6 demonstrates that all these regimes persist across multiple deployment seasons.

B. Consistency of dominant azimuth across frequency, year, and location

Figures 7–9 show that the median dominant azimuth measured by the DASARs is relatively consistent across deployment season and frequency at a particular location. The spread in this azimuth, as measured by the circular IQR, rises substantially as the transport velocity decreases. For a fixed value of transport velocity, the dominant azimuth IQR rises slightly with increasing frequency.

The dominant azimuth measured by the ambient sound field is consistent across a wide swath of frequencies, as long as U_c is measured at a sufficiently high level. For example, the median azimuth differs by just 10° (180°–190°) across the entire bandwidth on DASAR 5 G in 2014 [Fig. 7(a)], for U_c values between 0.6 and 0.95. The IQR of the azimuth ranges between 20° and 40° over most of this bandwidth.

In general, whenever the ambient field is associated with a high transport velocity, the acoustic energy is arriving from the north and propagating south. Across all three DASARs at Site 5 in 2014 (Fig. 7), ambient noise energy propagated toward a median compass azimuth between 180° and 190° (propagating from azimuths of 0° and 10°), regardless of frequency, whenever U_c was above 0.5. In 2010 (Fig. 8), the results were similar, except that energy propagated toward a median azimuth between 190° and 200°. Site 3 (Fig. 9) also displays similar features, although the corresponding directions are 190 and 220° (propagating from azimuths between 10° and 40°), and the IQR is slightly lower (30°) at frequencies below 100 Hz. DASAR 3 G also measures a median dominant azimuth [Fig. 9(a)] that is 10° greater than the DASAR B and D results [Fig. 9(b) and 9(c)].

As U_c decreases, the IQR of the median azimuth distribution widens substantially [e.g., 150° when $Uc = 0.2$ in Fig. 7(a)]. However, the median dominant azimuth of the acoustic field remains relatively consistent between 50 and ~250 Hz, even under these low-directionality conditions. However, above 300 Hz, the median azimuth of samples with low transport velocities can vary considerably between individual DASARs at a site, with energy arriving from directions other than north.

C. Speculations on relevance for human and marine life

The long-term stability of the dominant azimuth across multiple locations and years, along with the low IQR,

suggests that under certain conditions, vector sensor measurements in the Arctic can be used as a navigational aid. By monitoring both the normalized transport velocity and dominant azimuth of the low-frequency ambient sound field, a sensor could estimate the direction of true north, with confidence intervals. For situations when the measured transport velocity is high, the 50% confidence interval (IQR) can be within 40°, a more reliable measurement than a magnetic compass at these high latitudes.

Why, in this environment, would the ambient sound field have a consistent northern directionality during relatively low ambient noise conditions? As reviewed in the Introduction, the Beaufort Sea experiences little shipping traffic or surf noise, which means that the dominant source mechanism is surface agitation by wind (and occasionally, biological activity during some seasons). When the local winds over the sensor are strong, surface noise is generated at all azimuths surrounding the sensor, so the directionality, and thus, transport velocity of the resulting field is small, even if the power spectral density levels are high due to the close ranges of the surface agitation. However, if no local strong surface agitation exists, the effective surface region contributing to the sound field expands to much greater ranges. Unobstructed stretches of ocean exist to the east and west of the deployment site, and thus propagating ambient energy arriving from the east and west balance each other out, creating a relatively low component of the active intensity parallel to the Alaskan coast. However, the presence of this same landmass to the south implies that more ocean surface area north of the sensor is available to interact with the wind. Given the lack of noise generated by surf to the south, the resulting net acoustic energy should propagate from north to south, toward the shoreline. Since this energy flow arises from geography, the long-term properties of the ambient noise field should be stable. Because propagating low-frequency sound is generally less attenuated with distance, the effect is more enhanced at lower frequencies.

This interpretation suggests that two sensors deployed at different distances from shore should experience different transport velocities during calm ocean conditions, but cross-comparisons between DASARs across a site found ambiguous evidence of such an effect. Figure 5, which plots the relationship between ambient PSD level and transport velocity, finds that, for a fixed PSD level, DASAR G displays different transport velocities than A and C, but no such differences can be discerned between A and C. As the latter are separated by only 7 km, any potential difference in transport velocity may be too small to discern.

These results may provide a glimpse into the nature of ambient noise directionality along other continental coastlines during preindustrial times, when low-frequency distant shipping noise was absent. Previous literature has speculated that surf noise may have served as a navigational aid to migrating marine mammals along coasts, such as humpback and gray whales (Cotter, 2009). Most marine biologists believe that baleen whales can sense the arrival direction of low-frequency sounds, since most baleen whales produce sounds below 100 Hz. Recent finite-element modeling suggests that large baleen whales may be able to sense the directionality of sounds with frequencies as low as 10 Hz, if bone conduction through the skull is considered (Cranford and Krysl, 2018). These results raise the possibility that even in the absence of pounding surf, the underwater ambient sound field could still have embedded navigational cues for marine life in preindustrial times and may even serve such a role in the Arctic today—at least until commercial shipping traffic increases in response to retreating ice coverage arising from climate change.

VI. CONCLUSION

Low-frequency ambient sound generated during open-water arctic conditions along the Alaskan North Slope displays two regimes that are invisible to standard hydrophone measurements, but are associated with specific power spectral density ranges. Very high PSD levels are associated with highly directional discrete sources, like seismic airgun surveys or whale calls. Intermediate PSD levels are associated with low directionality and low transport velocity, consistent with local close-range wind-driven surface agitation typical of storms. Finally, at still lower PSD levels (which occurred at roughly one-half and one-third of the deployment time at 100 Hz and 350 Hz, respectively) the diffuse ambient sound field becomes highly directional again, despite the lack of individual discrete sources. The geometry of the Alaskan coast is proposed as an explanation of the southerly transport of ambient acoustic energy towards the shoreline. The consistency of the northerly arrival direction of this low-frequency energy across multiple years, locations, and frequencies raises the possibility that this ambient noise field can be used as an "acoustic compass" to provide navigational orientation data, whenever the measured normalized transport velocity exceeds 0.5. Projected increases in shipping activity in these arctic waters may eventually destroy this feature of the low-frequency ambient sound field.

The work to date has concentrated on open-water conditions, but limited DASAR data do exist to examine the potential impact of widespread ice floe coverage on the ambient noise directionality. Further theoretical analyses are needed to explain why distributions of intensity phase cluster around 45° in Fig. 3 during low-transport velocity conditions.

ACKNOWLEDGEMENTS

The authors wish to thank SEPCO for permission to use this dataset as well as the crews of the *Norseman II*, *Alpha Helix*, and *Westward Wind*, particularly deck chief Scotty Hameister, for consistently safe and professional deployments and retrievals of the DASARs over the project's lifetime. Dr. A. Michael Macrander provided strong leadership and guidance to the project, while Sheyna Wisdom and her colleagues at Fairweather LLC provided high-quality fieldwork logistical support. Two reviewers

provided comments that enhanced the manuscript quality. Finally, none of this work would have existed if Dr. Charles R. Greene, Jr. hadn't had the vision to deploy DASARs off the Beaufort coast two decades ago. Analyses of these data were supported by the Office of Naval Research (ONR) grant N00014-18-1-2064.

Aulanier, F., Simard, Y., Roy, N., Gervaise, C., and Bandet, M. (**2017**). "Effects of shipping on marine acoustic habitats in Canadian Arctic estimated via probabilistic modeling and mapping," Mar. Pollut. Bull. **125**, 115–131.

Blackwell, S. B., Nations, C. S., McDonald, T. L., Thode, A. M., Mathias, D., Kim, K. H., Greene, C. R., Jr., and Macrander, A. M. (**2015**). "The effects of airgun sounds on bowhead whale calling rates: Evidence for two behavioral thresholds," PLOS One **10**, e0125720.

Clark, C. W., Berchok, C. L., Blackwell, S. B., Hannay, D. E., Jones, J., Ponirakis, D., and Stafford, K. M. (**2015**). "A year in the acoustic world of bowhead whales in the Bering, Chukchi and Beaufort seas," Prog. Oceanogr. **136**, 223–240.

Cotter, A. J. R. (**2009**). "The 'soundscape' of the sea, underwater navigation, and why we should be listening more," Adv. Fish. Sci. **50**, 451–471.

Cranford, T. W., and Krysl, P. (**2018**). "Sound paths, cetaceans," in *Encyclopedia of Marine Mammals*, edited by B. Würsig, J. G. M. Thewissen, and K. Kovacs (Academic Press/Elsevier, San Diego, CA), pp. 963–966.

Cray, B. A., and Nuttall, A. H. (**2001**). "Directivity factors for linear arrays of velocity sensors," J. Acoust. Soc. Am. **110**, 324–331.

Cummings, W. C., and Holliday, D. V. (**1987**). "Sounds and source levels from bowhead whales off Pt. Barrow, Alaska," J. Acoust. Soc. Am. **82**(3), 814–821.

D'Spain, G. L., Hodgkiss, W. S., and Edmonds, G. L. (**1991**). "Energetics of the deep ocean's infrasonic sound field," J. Acous. Soc. Am. **89**(3), 1134–1158.

D'Spain, G. L., Luby, J. C., Wilson, G. R., and Gramann, R. A. (**2006**). "Vector sensors and vector sensor line arrays: Comments on optimal array gain and detection," J. Acoust. Soc. Am. **120**(1), 171–185.

Dahl, P. H., and Dall'Osto, D. R. (**2020**). "Estimation of seabed properties and range from vector acoustic observations of underwater ship noise," J. Acoust. Soc. Am. **147**, EL345–EL350.

Dall'Osto, D. R., Dahl, P. H., and Woong Choi, J. (**2012**). "Properties of the acoustic intensity vector field in a shallow water waveguide," J. Acoust. Soc. Am. **131**, 2023–2035.

Deal, T. J. (**2018**). "Vector sensor cross-spectral density for surface noise in a stratified ocean—Formulas for arbitrary sensor geometries," J. Acoust. Soc. Am. **143**, 605–615.

Delarue, J., Laurinolli, M., and Martin, B. (**2009**). "Bowhead whale (*Balaena mysticetus*) songs in the Chukchi Sea between October 2007 and May 2008," J. Acoust. Soc. Am. **126**, 3319–3328.

Diachok, O. I., and Winokur, R. S. (**1974**). "Spatial variability of underwater ambient noise at arctic ice-water boundary," J. Acoust. Soc. Am. **55**, 750–753.

Greene, C. R., McLennan, M. W., Norman, R. G., McDonald, T. L., Jakubczak, R. S., and Richardson, W. J. (**2004**). "Directional frequency and recording (DIFAR) sensors in seafloor recorders to locate calling bowhead whales during their fall migration," J. Acoust. Soc. Am. **116**, 799–813.

Guerra, M., Thode, A., Blackwell, S. B., and Macrander, M. A. (**2011**). "Quantifying seismic survey reverberation off the Alaskan North Slope," J. Acoust. Soc. Am. **130**, 3046–3058.

Halliday, W., Insley, S., Hilliard, R., de Jong, T., and Pine, M. (**2017**). "Potential impacts of shipping noise on marine mammals in the western Canadian Arctic," Mar. Pollut. Bull. **123**, 73–82.

Hawkes, M., and Nehorai, A. (**2003**). "Wideband source localization using a distributed acoustic vector-sensor array," IEEE Trans. Signal Process. **51**, 1479–1491.

Holler, R. A. (**2014**). "The evolution of the sonobuoy from World War II to the Cold War," U.S. Navy J. Underwater Acoust. **62**, 322–347.

Ivanova, S., Kessel, S., Espinoza, M., McLean, M., O'Neill, C., Landry, J., Hussey, N., Williams, R., Vagle, S., and Fisk, A. (**2020**). "Shipping alters the movement and behavior of Arctic cod (Boreogadus saida), a keystone fish in Arctic marine ecosystems," Ecol. Appl. **30**, e02050.

Johannessen, O. M., Sagen, H., Sandven, S., and Stark, K. V. (**2003**). "Hotspots in ambient noise caused by ice-edge eddies in the Greenland and Barents Seas," IEEE J. Ocean. Eng. **28**, 212–228.

Kinsler, L. E., Frey, A. R., Coppens, A. B., and Sanders, J. V. (**1982**). *Fundamentals of Acoustics* (John Wiley and Sons, New York, NY).

Lewis, J. K. (**1994**). "Relating arctic ambient noise to thermally-induced fracturing of the ice pack," J. Acoust. Soc. Am. **95**, 1378–1385.

MacIntyre, K. Q., Stafford, K. M., Berchok, C. L., and Boveng, P. L. (**2013**). "Year-round acoustic detection of bearded seals (*Erignathus barbatus*) in the Beaufort Sea relative to changing environmental conditions, 2008–2010," Polar Biol. **36**, 1161–1173.

Makris, N. C., and Dyer, I. (**1991**). "Environmental correlates of arctic ice-edge noise," J. Acoust. Soc. Am. **90**, 3288–3298.

Mann, J. A. III, Tichy, J., and Romano, A. J. (**1987**). "Instantaneous and time-averaged energy transfer in acoustic fields," J. Acoust. Soc. Am. **82**, 17–30.

Milne, A. R., and Ganton, J. H. (**1964**). "Ambient noise under arctic sea-ice," J. Acoust. Soc. Am. **36**, 855–857.

Nehorai, A., and Paldi, E. (**1994**). "Vector-sensor array processing for electromagnetic source localization," IEEE Trans. Signal Process. **42**, 376–398.

Oppenheim, A. V., and Schafer, R. W. (**1989**). *Discrete-Time Signal Processing* (Prentice Hall, Englewood Cliffs, NJ).

Raghukumar, K., Chang, G., Spada, F., and Jones, C. (**2020**). "A vector sensor-based acoustic characterization system for marine renewable energy," J. Mar. Sci. Eng. **8**, 187–198.

Schiffrer, G., and Stanzial, D. (**1994**). "Energetic properties of acoustic fields," J. Acoust. Soc. Am. **96**, 3645–3653.

Shi, J., Dosso, S. E., Sun, D., and Liu, Q. (**2019**). "Geoacoustic inversion of the acoustic-pressure vertical phase gradient from a single vector sensor," J. Acoust. Soc. Am. **146**, 3159–3173.

Shipps, J. C., and Deng, K. (**2003**). "A miniature vector sensor for line array applications," in *Oceans 2003. Celebrating the Past … Teaming Toward the Future* (IEEE, Piscataway, NJ), Vol. 5, pp. 2367–2370.

Stafford, K. M., Moore, S. E., Laidre, K. L., and Heide-Jørgensen, M. P. (**2008**). "Bowhead whale springtime song off West Greenland," J. Acoust. Soc. Am. **124**, 3315–3323.

Stein, P. J., Lewis, J. K., Parinella, J. C., and Euerle, S. E. (**2000**). "Under-ice noise resulting from thermally induced fracturing of the arctic ice pack: Theory and a test case application," J. Geophys. Res. Oceans **105**, 8813–8826, https://doi.org/10.1029/2000JC900009.

Tervo, O. M., Parks, S. E., Christoffersen, M. F., Miller, L. A., and Kristensen, R. M. (**2011**). "Annual changes in the winter song of bowhead whales (*Balaena mysticetus*) in Disko Bay, Western Greenland," Mar. Mamm. Sci. **27**, E241–E252.

Thode, A., Skinner, J., Scott, P., Roswell, J., Straley, J., and Folkert, K. (**2010a**). "Tracking sperm whales with a towed acoustic vector sensor," J. Acoust. Soc. Am. **128**, 2681–2694.

Thode, A. M., Blackwell, S. B., Conrad, A. S., Kim, K. H., Marques, T., Thomas, L., Oedekoven, C. S., Harris, D., and Bröker, K. (**2020**). "Roaring and repetition: How bowhead whales adjust their call density and source level (Lombard effect) in the presence of natural and seismic airgun survey noise," J. Acoust. Soc. Am. **147**, 2061–2080.

Thode, A., Kim, K. H., Greene, C. R., Jr., and Roth, E. (**2010b**). "Long range transmission loss of broadband seismic pulses in the Arctic under ice-free conditions," J. Acoust. Soc. Am. **128**, EL181–EL187.

Thode, A. M., Kim, K. H., Norman, R. G., Blackwell, S. B., and Greene, C. R., Jr. (**2016**). "Acoustic vector sensor beamforming reduces masking from underwater industrial noise during passive monitoring," J. Acoust. Soc. Am. **139**, EL105–EL111.

Thode, A. M., Sakai, T., Michalec, J., Rankin, S., Soldevilla, M. S., Martin, B., and Kim, K. H. (**2019**). "Displaying bioacoustic directional information from sonobuoys using 'azigrams,' " J. Acoust. Soc. Am. **146**, 95–102.

Uscinski, B. J., and Wadhams, P. (**1999**). "Ice-ocean acoustic energy transfer: Ambient noise in the ice-edge region," Deep Sea Res. Part II Top. Stud. Oceanogr. **46**, 1319–1333.

Wilson, O., Jr., Wolf, S. N., and Ingenito, F. (**1985**). "Measurements of acoustic ambient noise in shallow water due to breaking surf," J. Acoust. Soc. Am. **78**, 190–195.